CMS Physics Analysis Summary

Contact: cms-pag-conveners-exotica@cern.ch 2021/07/15

Search for long-lived particles decaying to displaced leptons in proton-proton collisions at $\sqrt{s} = 13$ TeV

The CMS Collaboration

Abstract

A search for new long-lived particles decaying to leptons is presented using proton-proton collisions produced by the CERN LHC at a center-of-mass energy of 13 TeV. Events are selected with two leptons (an electron [e] and a muon [μ], two electrons, or two muons) that both have transverse impact parameter values between 0.01 cm and 10 cm. Data used for the analysis were collected by the CMS detector in 2016, 2017, and 2018, and correspond to an integrated luminosity of 113 fb^{-1} for the eμ and $\mu\mu$ channels and 118 fb^{-1} for the ee. The search is designed to be sensitive to a wide range of models with nonprompt eμ, ee, and $\mu\mu$ final states. The results are interpreted with models involving top squarks that decay to displaced leptons via R-parity-violating interactions, a gauge-mediated supersymmetry breaking model with lepton superpartners that decay to gravitinos and displaced leptons, and a model involving exotic Higgs bosons that decay to long-lived scalars, which in turn decay to displaced leptons. This is the first search at CMS for displaced leptons at a center-of-mass energy of 13 TeV, and the first search at CMS for displaced leptons in the ee and $\mu\mu$ channels that does not require the leptons to come from a common displaced vertex.

1 Introduction

To date, no direct evidence of particles beyond the standard model (BSM) has been found by the CERN LHC experiments or any other facilities. However, the vast majority of LHC searches assume the lifetimes of new particles are short enough that their decay products are prompt. Search strategies are often not optimized for particles with measurable lifetimes whose decays produce displaced signatures in the detectors. Therefore, new phenomena with displaced signatures can escape such searches and be less constrained by the current results. BSM particles with long lifetimes can be produced for the same reasons that long-lived particles in the standard model are produced, namely, because of small couplings between the long-lived particles and lighter states, approximate symmetries that stabilize the particles' lifetimes, or limited phase space available for decays.

While the majority of searches are only sensitive to models that predict new phenomena with prompt signatures, both the CMS and ATLAS Collaborations have performed dedicated searches for decays of BSM particles with long lifetimes. Direct search strategies include finding BSM particles via anomalous energy loss and/or low velocity [1, 2] or via a disappearing track signature [3–5]. There are also numerous indirect searches targeting the decay products of long-lived particles, such as nonprompt final-state jets [6–10], photons [11, 12], leptons [13–17], or combinations thereof [18, 19]. These searches are often complementary, providing sensitivity to different ranges of particle lifetimes.

The CMS Collaboration has previously performed a search in a final state with one displaced electron (e) and one displaced muon (μ), using pp collision data recorded at a center-of-mass energy of 8 TeV [20]. The previous analysis and the current one, which uses data recorded at a center-of-mass energy of 13 TeV, are both optimized to the phase space just beyond the sensitivity of prompt searches but with smaller displacements than other searches for long-lived BSM signatures. As a result, this search is sensitive to long-lived particles with lifetimes between approximately 10^{-4} and 100 ns. These two analyses are unique in that they do not require that the displaced final-state particles originate from a common vertex. Such a vertex is often required in other searches under the assumption that a long-lived particle will decay to multiple leptons. In contrast, we here perform an inclusive search for displaced leptons that is sensitive to long-lived particle decays to one or more leptons. The search described in this note uses data taken with the CMS detector during 2016, 2017, and 2018. We conduct a search for long-lived particle decays in which there are one electron and one muon, two electrons, or two muons in the final state, where both of the leptons are displaced from the nominal proton-proton (pp) collision interaction point (IP). With respect to the previous search, this search has about a factor of 6 more integrated luminosity, it is performed at a higher center-of-mass energy, and it adds two same-flavor channels corresponding to the ee and $\mu\mu$ final states.

This search is designed to be model independent and to be sensitive to as many event topologies as possible. Consequently, the event selection focuses exclusively on a displaced, isolated dilepton signature and does not try to identify signal events using hadronic activity or missing transverse momentum from undetected particles leaving the detector. In this way, we retain sensitivity to any model that can produce leptons with displacements on the order of 0.01 cm to 10 cm, regardless of whether these leptons are accompanied by jets, missing transverse momentum, or other interesting kinematic features.

We interpret the search results in the context of several models with displaced leptons in the final state, the Feynman diagrams for which are shown in Fig. 1. The first model introduces R-parity-violating (RPV) terms in the superpotential of the minimally supersymmetric (SUSY) standard model [21], allowing the lightest SUSY particle (LSP) to decay to standard model (SM)

particles. Only lepton-number-violating operators are considered in order to avoid constraints from measurements of the lifetime of the proton [22]. With sufficiently small couplings for these operators, the LSP has a long enough lifetime that its decay products are measurably displaced from the pp interaction region. We focus on the case in which the LSP is the top squark ($\widetilde{\mathrm{t}}$), the superpartner of the top quark. At the LHC, the top squark would be dominantly pair produced, and we generate its decay through an RPV vertex to a b (d) quark and a lepton ℓ via $\widetilde{\mathrm{t}} \to \mathrm{b}\ell$ ($\widetilde{\mathrm{t}} \to \mathrm{d}\ell$). We have added the $\widetilde{\mathrm{t}} \to \mathrm{d}\ell$ decay to facilitate reinterpreting the results of this search, although we find that this decay mode produces similar results as those from the $\widetilde{\mathrm{t}} \to \mathrm{b}\ell$ decay. For simplicity, we assume lepton universality in the top squark decay vertex, so that the branching fraction to any lepton flavor, namely, an electron, muon, or tau lepton (τ), is equal to one-third. We also interpret the results with a gauge-mediated SUSY breaking (GMSB) model in which the next-to-lightest SUSY particle (NLSP) is long lived because of its small gravitational coupling to the LSP gravitino $\widetilde{\mathrm{G}}$, which is nearly massless [23]. In this model, the NLSP is the superpartner of a lepton (slepton) $\widetilde{\ell}$; we consider selectrons $\widetilde{\mathrm{e}}$, smuons $\widetilde{\mu}$, and staus $\widetilde{\tau}$ separately as well as together as co-NLSPs. The sleptons would be pair produced at the LHC and which would decay to a lepton (e, μ, or τ) of the same flavor and a gravitino. In addition, we consider a model that produces BSM Higgs bosons (H) through gluon-gluon fusion [24]. The H decays to two long-lived scalars S, each of which decays to two oppositely charged and same flavor leptons, which have an equal probability of being an electron or a muon, for simplicity. For the scenarios where the long-lived top squarks and sleptons decay to tau leptons, the tau leptons are allowed to decay leptonically to electrons or muons.

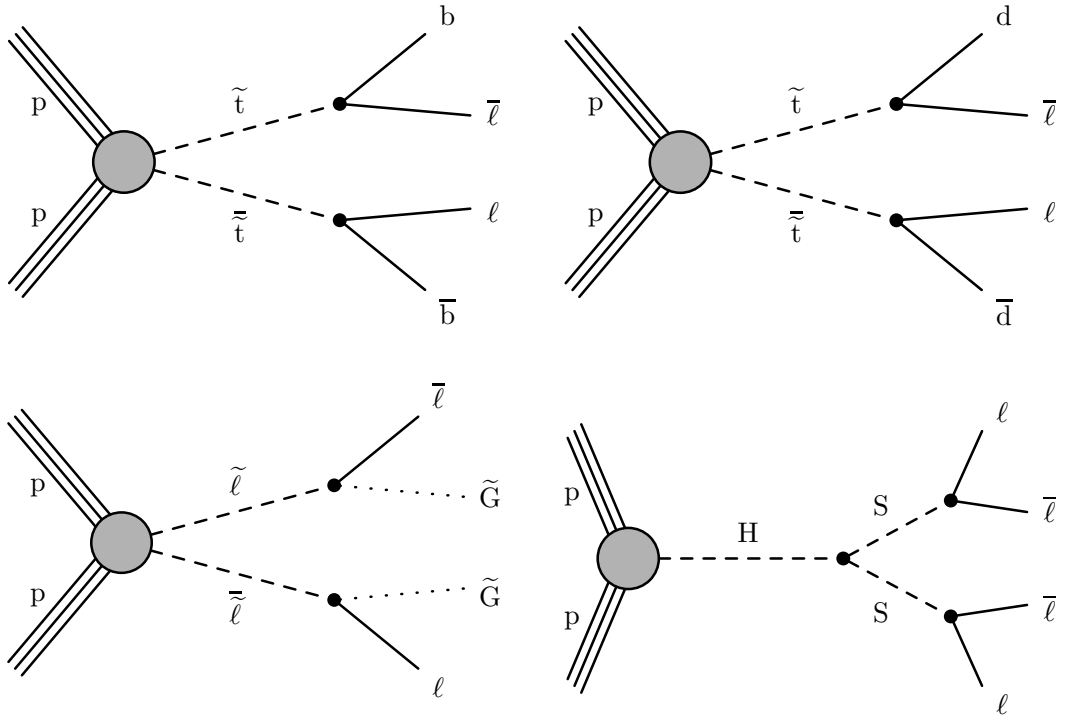

Figure 1: Feynman diagrams for $\widetilde{\mathrm{t}}\bar{\widetilde{\mathrm{t}}} \to \bar{\ell}\mathrm{b}\,\ell\bar{\mathrm{b}}$ (upper left), $\widetilde{\mathrm{t}}\bar{\widetilde{\mathrm{t}}} \to \bar{\ell}\mathrm{d}\,\ell\bar{\mathrm{d}}$ (upper right), $\widetilde{\ell}\bar{\widetilde{\ell}} \to \bar{\ell}\widetilde{\mathrm{G}}\,\ell\widetilde{\mathrm{G}}$ (lower left), and $\mathrm{H} \to \mathrm{SS} \to \ell\bar{\ell}\,\ell\bar{\ell}$ (lower right).

2 The CMS detector

The central feature of the CMS apparatus is a superconducting solenoid of 6 m internal diameter, providing a magnetic field of 3.8 T. Within the solenoid volume are a silicon pixel and strip tracker, a lead tungstate crystal electromagnetic calorimeter (ECAL), and a brass and scintillator hadron calorimeter (HCAL), each composed of a barrel and two endcap sections. The electron momentum is estimated by combining the energy measurement in the ECAL with the momentum measurement in the tracker. Forward calorimeters extend the pseudorapidity coverage provided by the barrel and endcap detectors. Muons are detected in gas-ionization chambers embedded in the steel flux-return yoke outside the solenoid using three technologies: drift tubes (DTs) in the barrel, cathode strip chambers (CSCs) in the endcaps, and resistive-plate chambers in both the barrel and the endcaps. Each of the four muon stations provides reconstructed hits on several detection planes, which are combined into local track segments, forming the basis of muon reconstruction inside the muon system.

The silicon tracker measures charged particles within the pseudorapidity range $|\eta| < 3.0$. During the 2016 LHC run, the silicon tracker consisted of 1440 silicon pixel and 15 148 silicon strip detector modules. The pixel detector was then upgraded, such that in the 2017 and 2018 LHC runs, it consisted of 1856 pixel modules [25]. For nonisolated particles of $1 < p_{\mathrm{T}} < 10\,\mathrm{GeV}$ and $|\eta| < 3.0$, the track resolutions are typically 1.5% in p_{T} and 20–75 μm in the transverse impact parameter (d_0), defined as the distance of closest approach in the transverse plane of the helical trajectory of the track with respect to the center of the luminous region [26, 27]. The sign of d_0 is given by the sign of the dot product between the lepton momentum and the vector between the center of the luminous region and the lepton track reference point. The d_0 resolution is approximately 25% smaller than in earlier data sets, thanks to the silicon pixel tracker upgrade. The efficiency to reconstruct tracks as function of $|d_0|$ is given in Ref. [27]. The analysis is sensitive up to 10 cm in lepton track $|d_0|$ because the outermost silicon pixel layer was at a radius of about 10 cm in 2016.

Events of interest are selected using a two-tiered trigger system. The first level, composed of custom hardware processors, uses information from the calorimeters and muon detectors to select events at a rate of around 100 kHz within a fixed latency of about 4 μs [28]. The second level, known as the high-level trigger (HLT), consists of a farm of processors running a version of the full event reconstruction software optimized for fast processing, and reduces the event rate to around 1 kHz before data storage [29, 30].

A more detailed description of the CMS detector, together with a definition of the coordinate system used and the relevant kinematic variables, can be found in Ref. [31].

3 Data and Monte Carlo simulation

The data correspond to an integrated luminosity of $113\,\mathrm{fb}^{-1}$ for the eμ and $\mu\mu$ channels and $118\,\mathrm{fb}^{-1}$ for the ee channel. The difference in integrated luminosity in the different channels is due to the availability of the triggers, which will be described in the next section. In addition, we use events containing muons from cosmic ray showers, which were recorded with dedicated triggers, as a control sample to evaluate the tracking efficiency of displaced particles, as will be described later.

In the Monte Carlo (MC) simulation of background and signal processes, minimum-bias interactions are superimposed on each event to simulate the effect of overlapping interactions within the same event (pileup), as observed in data. The average number of pileup interactions

was 23 (32) in 2016 (2017 and 2018). The NNPDF 3.0 [32] parton distribution functions are used in all generated samples. The modeling of the underlying event uses the CUETP8M1 [33] and CP5 tunes [34] for simulated samples corresponding to the 2016 and 2017–2018 data sets, respectively. The MC-generated events are then processed through a detailed simulation of the CMS detector based on GEANT4 [35] and are reconstructed with the same algorithms used for data.

While the background is estimated with a fully data-driven technique, simulated background samples are produced to perform basic checks such as data-to-simulation comparisons in control regions. The samples simulating Z+jets, W+jets, and $\mathrm{t\bar{t}}$ production are generated at leading order using MADGRAPH5_aMC@NLO v2 [36, 37] and the MLM merging scheme [38], while those simulating diboson and single-top-quark production are simulated at next-to-leading order with POWHEG v2 [39–43]. PYTHIA 8.2 [44] is used to simulate the parton showering and hadronization for all processes. Samples of the signal process $\mathrm{pp} \to \widetilde{\mathrm{t}}\bar{\widetilde{\mathrm{t}}}$, with the top squarks decaying via $\widetilde{\mathrm{t}} \to \mathrm{b}\ell$ or $\widetilde{\mathrm{t}} \to \mathrm{d}\ell$ are generated using PYTHIA 8.2 at leading order. The top squarks can form strongly produced hadronic states called "R-hadrons," which are generated with PYTHIA. In the samples used in this analysis, the interactions of the R-hadrons with matter are not simulated in GEANT4. However, such interactions are not expected to have a significant impact because these particles do not traverse a significant number of interaction lengths before decaying. Nevertheless, we study the impact of the R-hadron interactions using the "cloud model," which assumes that the top squark is surrounded by a cloud of colored, light constituents that interact during scattering [45, 46], and find the effect on the signal efficiency to be negligible. The GMSB sleptons are generated at leading order using MADGRAPH5_aMC@NLO v2.6.5 and PYTHIA 8.2, and the slepton decay via $\widetilde{\ell}\bar{\widetilde{\ell}} \to \bar{\ell}\widetilde{\mathrm{G}}\,\ell\widetilde{\mathrm{G}}$ is simulated using GEANT4, which does not preserve information about the chirality of the slepton. The signal process $\mathrm{pp} \to \mathrm{H} \to \mathrm{SS} \to \ell\bar{\ell}\,\ell\bar{\ell}$ is generated using POWHEG v2 and PYTHIA 8.2 at next-to-leading order.

4 Analysis strategy

We perform an inclusive search for displaced leptons by selecting events with good quality electrons and muons, and by rejecting background events from SM processes that produce displaced leptons, as will be described in Section 5. We use the lepton $|d_0|$, which is the main discriminating variable in the analysis, to define the signal regions (SRs). Using data in a prompt control region, we correct the $|d_0|$ distributions in background and signal simulation to account for alignment and resolution effects not fully modeled in simulation, as will be described in Section 6. We perform a fully data-driven background estimate, using the lepton $|d_0|$ to separate signal-like events from background-like ones, as will be described in Section 7. The lepton $|d_0|$ for the signal processes is modeled with simulation, so we validate the modeling of the displaced tracking efficiency in data using displaced muons from cosmic ray events. From these studies, we derive systematic uncertainties that are applied to the signal, as will be described in Section 8.

5 Event reconstruction and selection

Events were recorded with different triggers in each of the three channels. Because standard CMS electron triggers are not designed to recognize displaced tracks, we use photon triggers instead to ensure efficiency for finding displaced electrons. In fact, photon HLT paths efficiently select electrons as well, as these triggers do not veto electrons or charged particle tracks. In

the eμ channel, the trigger requires at least one muon without any constraints to the primary pp interaction vertex and without any maximum $|d_0|$ requirement, and at least one photon. In 2016, the muon and photon are both required to have transverse momentum $p_T > 28$ GeV if the muon $|d_0|$ is greater than 0.01 cm and $p_T > 38$ GeV otherwise. In 2017 and 2018, the muon and photon are both required to have $p_T > 43$ GeV; the p_T threshold is increased during these years to combat the increased pileup. In the ee channel, the events are required to pass the logical OR of two high-level triggers. The first trigger requires the largest transverse energy photon to have transverse energy $E_T > 30$ GeV and the second largest E_T photon to have $E_T > 18$ (22) GeV in 2016 (2017 and 2018). Calorimeter identification and isolation requirements are made on both photons, and the fraction of the photon energy in the ECAL divided by that in the HCAL is required to be large. In addition, the diphoton invariant mass must be >90 GeV. The second trigger simply requires at least two photons with $E_T > 60$ (70) GeV in 2016 (2017 and 2018). In the $\mu\mu$ channel, the trigger requires at least two muons without any primary vertex constraints and without any maximum requirement on the impact parameter. In 2016, the muons are required to have $p_T > 23$ GeV if the muon $|d_0|$ is greater than 0.01 cm and $p_T > 33$ GeV otherwise. In 2017 and 2018, the muons are required to have $p_T > 43$ GeV. With these triggers, an efficiency of 20–40% is achieved, depending on signal mass, lifetime, and analysis channel.

After requiring that the events pass the triggers described above, we preselect well-reconstructed electrons and muons in each channel. Electrons and muons are reconstructed by associating a track reconstructed in the tracking detectors with either a cluster of energy in the ECAL [47, 48] or a track in the muon system [49]. The leptons used in this search are reconstructed with the particle-flow (PF) algorithm [50], which aims to reconstruct and identify each individual particle in an event with an optimized combination of information from the various elements of the CMS detector. The candidate vertex with the largest value of summed physics-object p_T^2 is taken to be the primary pp interaction vertex. The physics objects are the jets, clustered using the jet finding algorithm [51, 52] with the tracks assigned to candidate vertices as inputs, and the associated missing transverse momentum, taken as the negative vector sum of the p_T of those jets.

In the eμ channel, we preselect events with at least one PF electron and at least one PF muon, while in the same-flavor channels, we preselect events with at least two PF electrons or muons. In the eμ channel, we require the electrons to have $p_T > 42$ (45) GeV and the muons to have $p_T > 40$ (45) GeV in 2016 (2017 and 2018). In the ee channel, we require the electrons to have $p_T > 65$ (75) GeV, and in the $\mu\mu$ channel, we require the muons to have $p_T > 35$ (45) GeV. These p_T requirements are set at the point where the trigger efficiency has plateaued. In all three channels, we require the electrons and muons to have a pseudorapidity $|\eta| < 1.5$ in order to remove leptons with poorly measured $|d_0|$, which are predominantly at large $|\eta|$. Since signal leptons are predominantly central, this requirement has a minimal impact on the signal efficiency. In addition, electrons in the transition region between the barrel and the endcap detectors are rejected, which effectively means that electrons are required to have $|\eta| < 1.44$. We also reject electrons and muons in certain regions of the η-ϕ plane because two layers of the pixel tracker were not fully functional during certain data-taking periods, resulting in increased $|d_0|$ mismeasurements. The rejected regions are $1.0 < \eta < 1.5$, $\phi > 2.7$ in 2017 and $0.3 < \eta < 1.2$, $0.4 < \phi < 0.8$ in 2018. This requirement reduces the signal efficiency by <1%.

Identification requirements, based on energy deposits in the calorimeters and on hit information in the tracker and muon systems, are imposed on the electrons and muons at the "tight" working point [47–49]. Included in these identification requirements is the criterion that the innermost hit of the electron track must occur within the first two functional pixel layers tra-

versed by the electron. The identification requirements for muons include that each muon track must have at least one hit in the pixel detector, at least six tracker layer hits, and segments with hits in two or more muon detector stations.

To ensure that electrons and muons are isolated from other particles, we calculate the scalar sum of the p_T of all other particles within a cone of $\Delta R \equiv \sqrt{\Delta\eta^2 + \Delta\phi^2} < 0.3$ (0.4) around the electron (muon), correct this sum for contributions from pileup, and define the relative isolation as the ratio of this sum to the electron (muon) p_T. For each lepton, the pileup correction term is equal to the average energy per unit area in each event multiplied by the area of the isolation cone. Calculating the relative isolation in this way allows for the possibility that the displaced lepton is associated with the wrong primary vertex. We require that the relative isolation is <0.10 for muons, <0.0588 for electrons in 2016, and $<0.0287 + 0.506/p_T$ for electrons in 2017 and 2018.

Besides these object-level selections, we also impose a few event-level selections. To remove cosmic-ray muons in the $\mu\mu$ and eμ channels, we require that there are zero pairs of muons with $\cos\alpha < -0.99$, where α is the three-dimensional angle between the muons. This selection removes back-to-back muons, which is how cosmic-ray muons from the Earth's atmosphere appear in the detector, should they reach it. In addition, we require that the relative time between the leading (largest p_T) two muons is not consistent with the timing of cosmic-ray muons. To do this, we look at the muon time at the IP as measured by the DTs and CSCs, assuming the muons are outgoing. We then determine which muon is above the other based on their ϕ measurements, and find Δt, the time of the lower muon subtracted from the time of the upper muon. Since cosmic-ray muons traverse the detector from top to bottom, the lower muon appears later in time than the upper muon, assuming the muons are outgoing from the IP, making Δt negative for cosmic-ray muons. On the other hand, muons from the pp collision have similar times as they are both outgoing from the IP, and so they have a Δt distribution centered at 0 ns. We reject events with $\Delta t < -20$ ns if the number of degrees of freedom of the timing measurements for both muons is greater than seven. We also require that the relevant leptons in each channel are separated by $\Delta R > 0.2$. This loose requirement is sufficient to significantly reduce the contribution from the heavy-flavor background from B or D meson decays. In addition, we reject events where the candidate leptons form a good displaced vertex that overlaps with the tracker material, which is measured in Ref. [53]. The vertices are reconstructed with the Kalman vertex fitter [54, 55], and a "good" vertex is one with a resolution of less than 10 μm and a $\chi^2/N_{\text{dof}} < 20$, where N_{dof} is the number of degrees of freedom of the fit.

The events passing each channel preselection criteria are further categorized using the $|d_0|$ of the selected leptons. We define a "prompt control region" by requiring the electrons and muons to have $|d_0| < 50\,\mu$m. This region is dominated by standard model processes with prompt leptons and is used to check that the background simulation accurately reproduces the behavior of the data. The "inclusive signal region" is defined by requiring the electrons and muons have $100\,\mu\text{m} < |d_0| < 10$ cm. We do not select leptons that are displaced by more than 10 cm to ensure that the leptons originate within the pixel tracker, since the lepton identification criteria effectively require hits in at least one pixel layer.

To remove overlaps between the three channels, we reject events that would fall into the eμ inclusive signal region in the same-flavor channels. That is, in the ee ($\mu\mu$) channel, we reject events with at least one muon (electron) that passes the eμ channel preselection and has $|d_0| > 100\,\mu$m.

Table 1: The cumulative efficiency for $\widetilde{\mathrm{t}}\bar{\widetilde{\mathrm{t}}} \to \bar{\ell}\mathrm{b}\,\ell\bar{\mathrm{b}}$ signal events to pass the 2018 inclusive signal region selection, for several choices of $\widetilde{\mathrm{t}}$ mass and $c\tau_0$. The corrections described in Section 6 are applied.

	eμ signal region		
	200 GeV	1000 GeV	1800 GeV
0.1 cm	2.0%	4.5%	4.5%
1 cm	3.5%	7.8%	8.7%
10 cm	1.0%	2.6%	3.3%
100 cm	0.05%	0.12%	0.15%
	ee signal region		
	200 GeV	1000 GeV	1800 GeV
0.1 cm	0.45%	2.1%	2.1%
1 cm	0.59%	2.8%	3.3%
10 cm	0.11%	0.59%	0.76%
100 cm	0.002%	0.01%	0.02%
	μμ signal region		
	200 GeV	1000 GeV	1800 GeV
0.1 cm	1.4%	2.5%	2.5%
1 cm	3.0%	5.5%	5.8%
10 cm	1.4%	3.0%	3.6%
100 cm	0.10%	0.22%	0.31%

Table 1 shows the cumulative efficiency for $\widetilde{\mathrm{t}}\bar{\widetilde{\mathrm{t}}} \to \bar{\ell}\mathrm{b}\,\ell\bar{\mathrm{b}}$ events to pass the 2018 inclusive signal region selection for several choices of $\widetilde{\mathrm{t}}$ mass and proper decay length ($c\tau_0$), where c is the speed of light and τ_0 is the proper lifetime. The efficiencies are similar for each year of data taking. The larger signal efficiency in the eμ channel relative to either of the same-flavor channels is primarily due to simple combinatorics: two top squarks decaying with equal probability to an electron, a muon, or a tau lepton will produce an eμ final state twice as often as either of the same-flavor final states.

6 Corrections to the simulation

Several corrections are applied to the MC simulations in order to account for known differences between simulation and data. The simulation is corrected so that its distribution of pileup interactions matches that of 2016, 2017, and 2018 data. In addition, the trigger efficiency is measured in simulation and an independent data sample recorded with missing transverse momentum triggers, for the three years of data taking and for each analysis channel separately. The ratio of the trigger efficiency in data and simulation is applied as a "scale factor" on each lepton in the simulated samples. The scale factor is a weight applied to each lepton, so that in events with two leptons, the overall event weight is the product of the two lepton weights, assuming the leptons are independent. The average trigger scale factor for electrons (muons) is 0.982 ± 0.028 (0.931 ± 0.003). While these trigger scale factors are derived with samples dominated by prompt events, we also evaluate consistent scale factors using displaced lepton samples. Scale factors are also applied as a function of lepton p_{T} and η, in order to correct the performance of the lepton identification and isolation algorithms [47–49].

Separate scale factors are applied to each lepton in order to correct the simulated lepton $|d_0|$ distributions. The scale factors are derived by fitting the background and the data lepton d_0 distributions with Gaussian functions in each channel's prompt control region, and by then

comparing the widths of the Gaussian fits. The width of each Gaussian fit is largely set by the lepton d_0 resolution, and the discrepancy between the data and background MC simulation lepton d_0 distributions is due to an overly optimistic alignment in the simulation, which creates an unrealistically ideal d_0 resolution. Therefore, we define $\sigma^2_{\text{data}} = \sigma^2_{\text{bkg}} + \sigma^2_{\text{align}}$, where σ_{data} is the width of the fit in data, σ_{bkg} is the width in background simulation, and σ_{align} is the additional piece that is needed to make the background simulation and data agree in each channel's prompt control region. We find σ_{data} and σ_{bkg} from the fits, and compute σ_{align}. The fit results are similar in each channel, so we average the σ_{align} derived in the ee channel and the eμ channel for electrons, and in the $\mu\mu$ channel and the eμ channel for muons. We then smear the simulation d_0 distribution by picking random values within a Gaussian distribution centered at 0 and with a width of the average σ_{align}, and applying these random values as scale factors to each lepton. The average σ_{align} is 14.8 ± 0.4 (9.2 ± 0.4) μm for electrons and 7.6 ± 0.1 (8.1 ± 0.1) μm for muons in 2017 (2018). No $|d_0|$ scale factor is found to be needed for the simulation with 2016 data-taking conditions, as the simulation for 2016 data is already adjusted for the alignment. The scale factors are applied to both background and signal MC simulation.

7 Background estimation

Most leptons resulting from SM processes are from particles that decay promptly. However, displaced leptons can arise from a few different sources. Displaced leptons resulting from cosmic-ray muons, material interactions, and long-lived SM hadrons are largely rejected by the analysis selection criteria. In particular, the tight isolation criteria reject the vast majority of the heavy-flavor background. Nevertheless, leptons from mismeasurements of prompt tracks or from decays of tau leptons and B and D mesons, which have proper decay lengths of 87 μm, 500 μm, and less than 100 μm, respectively, may still appear in the SRs.

7.1 Data-driven ABCD method

To estimate the number of background events in the SRs, we employ a data-driven "ABCD method" that accounts for all three significant background sources: mismeasurements, tau lepton decays, and heavy-flavor decays. First, we categorize the events that pass the preselection criteria into four regions (A, B, C, and D) based on each lepton $|d_0|$ measurement, namely, $|d_0^{\text{a}}|$ and $|d_0^{\text{b}}|$, as shown in Fig. 2. For the eμ channel, $|d_0^{\text{a}}|$ is defined as the leading electron $|d_0|$ and $|d_0^{\text{b}}|$ is defined as the leading muon $|d_0|$. For the ee ($\mu\mu$) channel, $|d_0^{\text{a}}|$ is defined as the leading electron (muon) $|d_0|$ and $|d_0^{\text{b}}|$ is defined as the subleading electron (muon) $|d_0|$. We use the number of background events in regions A, B, and C to estimate the expected background in region D, which is the signal region. We assume that $N_{\text{B}}/N_{\text{A}} = N_{\text{D}}/N_{\text{C}}$ or that the number of background events in D is $N_{\text{B}}N_{\text{C}}/N_{\text{A}}$, where N_{X} is the number of background events in the given region. This assumption is valid if $|d_0^{\text{a}}|$ and $|d_0^{\text{b}}|$ are not correlated. We correct for deviations from this assumption as described below.

7.2 Signal regions (SRs)

We subdivide the inclusive signal region to define nonoverlapping SRs in $|d_0|$:

- SR I: $100 <$ both $|d_0| < 500\,\mu$m
- SR II: $100 < |d_0^{\text{a}}| < 500\,\mu$m, $500\,\mu\text{m} < |d_0^{\text{b}}| < 10\,$cm
- SR III: $500\,\mu\text{m} < |d_0^{\text{a}}| < 10\,$cm, $100 < |d_0^{\text{b}}| < 500\,\mu$m
- SR IV: $500\,\mu\text{m} <$ both $|d_0| < 10\,$cm

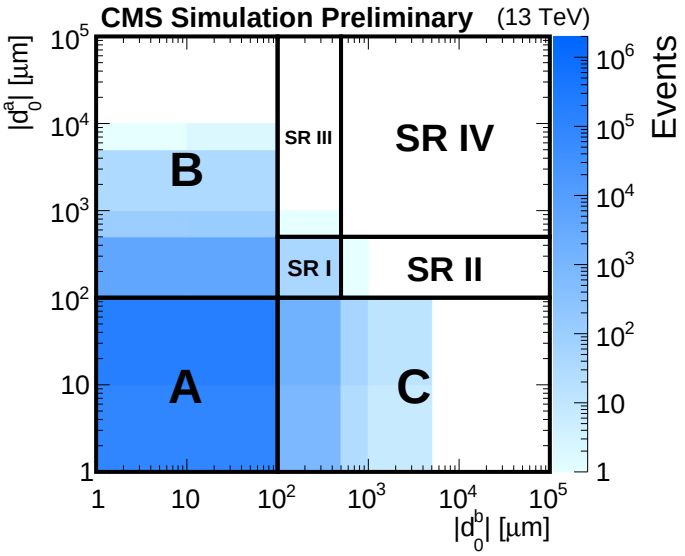

Figure 2: A diagram of the ABCD method, shown for illustration on background simulation passing the eμ preselection with 2018 conditions. If a $|d_0|$ value is less than unity, it is set to unity for plotting. A, B, and C are control regions, and D is the inclusive SR. SRs I–IV are described in the text below.

Dividing the inclusive SR in this way separates the expected contribution of different background sources into individual SRs and gives loose SRs with some amount of background contamination but high signal efficiency and tight SRs with little background contamination but also smaller signal efficiency. The signal efficiency in each SR depends on the lifetime of the new long-lived particle, so dividing the inclusive SR into multiple SRs also helps the search to be sensitive to a wide range of long-lived particle lifetimes. We also bin SR I, which has the largest number of expected background events, in one lepton's p_{T} in order to maximize sensitivity. Because they are nonoverlapping, we can use these SRs simultaneously in the limit-setting procedure.

We perform a separate ABCD estimate for each SR. When performing the estimates, we subdivide regions B and C into 100–500 μm and 500 μm–10 cm regions to match the SR definitions, and bin region A and the 100–500 μm subregions of B and C in p_{T} to match the binning of SR I.

7.3 Closure tests in one-prompt/one-displaced sidebands

The background estimation method nominally relies on the lepton $|d_0|$ values being uncorrelated. The preselection criteria remove one possible source of $|d_0|$ correlation by ensuring that leptons that share a common displaced vertex do not contribute meaningfully to the SRs, but $|d_0|$ correlation may still arise as a result of correlation in parentage between leptons. Specifically, we find that DY$\to\ \tau\tau$ events in which each tau lepton decays to an electron or muon lead to correlation in the lepton $|d_0|$ values. Flavor conservation correlates the lepton parentage, and because the tau lepton is long lived, the correlation in parentage leads to correlation in $|d_0|$. In principle, processes that produce pairs of B or D mesons could introduce $|d_0|$ correlation through this same mechanism, but the lepton isolation criteria ensure a negligible SR

contribution from events in which both leptons are produced in B or D meson decays. We therefore expect the degree of $|d_0|$ correlation to increase with the fraction of events from DY$\to \tau\tau$. Studies with simulation show that leptons from tau lepton decays contribute significantly from about 100 to 500 μm and peak around 200 μm, so we expect $|d_0|$ correlation to appear in this range and peak accordingly. The ability to measure such $|d_0|$ correlation depends on the quality of the $|d_0|$ measurement. Because $|d_0|$ resolution is better for muons than for electrons and is better in the 2017 and 2018 data-taking periods relative to the 2016 data-taking period, we also expect $|d_0|$ correlation to be more apparent in 2017 and 2018 and increase with the number of muons in the final state. We observe this $|d_0|$ correlation in the closure tests described below and correct for it using the procedure described in Section 7.4.

We perform closure tests in sideband regions with one prompt and one displaced lepton in data and background simulation. We first perform these closure tests in the region where the prompt (displaced) lepton has a displacement of 30–100 (100–500) μm. We use the estimated and actual yields in several subregions of each sideband region to estimate the ratio of the actual yield to the estimated yield in SR I. This procedure will be described more fully in Section 7.4. Table 2 shows the resulting ratios in data, background simulation, and background simulation with the DY$\to \tau\tau$ events removed. As expected, the ratios in data are frequently greater than unity, which indicates nonclosure of the ABCD method and positive $|d_0|$ correlation. The data ratios generally agree with those of the full background simulation, which indicates that the source of nonclosure is modeled in the background simulation. To test if DY$\to \tau\tau$ events are the source of nonclosure, we repeat the closure tests with DY$\to \tau\tau$ events removed from the simulation and find that the ratios are consistent with unity. Because the full simulation successfully models the observed nonclosure in data and because removing the DY$\to \tau\tau$ events results in closure, we conclude that DY$\to \tau\tau$ events are indeed the only meaningful source of $|d_0|$ correlation.

Table 2: Closure test results in data, background simulation, and background simulation with the DY$\to \tau\tau$ events removed in the 100–500 μm region. The extrapolated ratios of the actual yield to the estimated yield (averaged over the two one-prompt/one-displaced sidebands) and their statistical uncertainties are given.

	Data	Full Bkg. simulation	Bkg. simulation without DY$\to \tau\tau$
2016 eμ	0.9 ± 1.3	1.6 ± 0.6	0.9 ± 0.3
2017+2018 eμ	3.1 ± 0.8	1.6 ± 0.7	1.1 ± 0.4
2016 ee	0.6 ± 0.6	0.8 ± 0.5	0.8 ± 0.5
2017+2018 ee	1.5 ± 0.4	1.6 ± 0.9	0.8 ± 1.0
2016 $\mu\mu$	2.5 ± 0.9	2.0 ± 0.8	1.1 ± 0.8
2017+2018 $\mu\mu$	4.2 ± 1.5	7.8 ± 3.7	2.6 ± 2.8
Average	2.1 ± 0.4	2.6 ± 0.7	1.2 ± 0.5

We next perform closure tests in sideband regions where one lepton is prompt (30–100 μm) and the other is even more displaced (500 μm–10 cm). Table 3 shows the ratios of the actual yield to the estimated yield averaged over the two one-prompt/one-displaced sidebands in data, background simulation, and background simulation with the DY$\to \tau\tau$ events removed. In each case, the resulting ratios are consistent with unity, and data and background simulation agree. Thus, in contrast to the 100–500 μm region tests, the 500 μm–10 cm region tests show no evidence of $|d_0|$ correlation. We also note that removing the DY$\to \tau\tau$ events from the background simulation does not significantly affect the results, which provides further evidence that the background from tau lepton decays is subdominant in this region. We therefore conclude that $|d_0|$ correlation is significant in the 100–500 μm region and insignificant in the 500 μm–10 cm

region.

Table 3: Closure test results in data, background simulation, and background simulation with the DY$\to\ \tau\tau$ events removed in the 500 μm–10 cm region. The ratios of the actual yield to the estimated yield (averaged over the two one-prompt/one-displaced sidebands) and their statistical uncertainties are given.

	Data	Full Bkg. simulation	Bkg. simulation without DY$\to\ \tau\tau$
2016 eμ	$0.4^{+1.0}_{-0.4}$	$1.0^{+0.3}_{-0.2}$	$1.0^{+0.3}_{-0.2}$
2017+2018 eμ	$0.7^{+0.7}_{-0.4}$	$0.9^{+0.2}_{-0.1}$	$0.8^{+0.2}_{-0.2}$
2016 ee	$1.0^{+0.9}_{-0.5}$	$2.2^{+2.9}_{-1.6}$	$2.2^{+2.9}_{-1.5}$
2017+2018 ee	$1.0^{+0.2}_{-0.2}$	$1.2^{+1.3}_{-0.7}$	$2.0^{+1.4}_{-0.9}$
2016 $\mu\mu$	$0.7^{+0.3}_{-0.2}$	$1.0^{+0.3}_{-0.3}$	$0.9^{+0.3}_{-0.2}$
2017+2018 $\mu\mu$	$1.2^{+0.3}_{-0.4}$	$0.5^{+0.6}_{-0.2}$	$0.6^{+0.9}_{-0.4}$
Average	$0.8^{+0.3}_{-0.2}$	$1.1^{+0.5}_{-0.3}$	$1.3^{+0.6}_{-0.3}$

7.4 Correction to estimate and systematic uncertainty

We now define a procedure to account for the $|d_0|$ correlation in the ABCD method and assign a systematic uncertainty in the estimate. First, as is done in the closure tests, we divide each one-prompt/one-displaced sideband into two subregions in the displaced lepton $|d_0|$: (1) the 100–500 μm region, where we find correlation from tau leptons to be significant, and (2) the 500 μm–10 cm region, where we find correlation from tau leptons to be insignificant. The 100–500 μm (500 μm–10 cm) sideband region is used as a control region for SR I (SRs II–IV). We perform closure tests in data in each subregion and use the ratio of the actual to the estimated number of events as a measure of nonclosure. From the 500 μm–10 cm region tests, we take the largest deviation of the ratio from unity as a systematic uncertainty in SRs II–IV, and apply no correction. This is a conservative approach that produces a large systematic uncertainty in the small background estimates that we find in this region. When the displaced lepton $|d_0|$ is between 100 and 500 μm, we fit the ratio as a function of the prompt lepton $|d_0|$ with a straight line, where the slope and y-intercept are allowed to vary. We extrapolate the prompt lepton fit to 200 μm (within SR I), which is the value where simulation indicates we should expect the largest contribution from tau lepton decays. The center of mass of the 100–500 μm bin in the background simulation is also at approximately 200 μm. We take the average of the two extrapolated ratios (one from each one-prompt/one-displaced sideband) and derive a correction and systematic uncertainty from this average ratio. If the average is greater than unity, we use the average as a multiplicative correction to the background estimate, and we use the uncertainty in the average as a systematic uncertainty in the background estimate. In this case, we also vary the 200 μm extrapolation point by $\pm$50 μm, which is the approximate width of the tau lepton contribution as a function of $|d_0|$, and apply the variation in the resulting correction as an additional systematic uncertainty in the background estimate. If the average is less than or equal to unity, we set the correction equal to unity and use the uncertainty in the average as a symmetric systematic uncertainty about unity. The size of the correction varies between 1.0 ± 0.6 and 4.2 ± 1.8, depending on channel and year.

7.5 Closure tests in signal regions

To test the full background estimation procedure, we perform closure tests in background simulation in the four SRs, with all corrections and systematic uncertainties derived from background simulation. In these tests, both leptons are displaced. The results of these closure tests in the SRs are shown in Table 4 with the 2016 and 2017+2018 yields combined in each channel. The actual yields are generally compatible with the estimated yields, which indicates that the correction performs as expected and the systematic uncertainties are sufficient to cover any unforeseen correlation.

Table 4: Closure test results in background simulation in the SRs, with the correction applied. The estimated number of events, the actual number of events, and their total uncertainties (statistical plus systematic) are given. In cases where the actual number of events is zero, the uncertainty is given by the product of the average background simulation event weight and the upper bound of the 68% Poisson interval given by a single observation of zero events.

	SR I	SR II	SR III	SR IV
eμ estimated	21^{+8}_{-8}	$0.4^{+0.4}_{-0.4}$	$0.4^{+0.4}_{-0.4}$	$0.02^{+0.02}_{-0.02}$
eμ actual	24^{+12}_{-7}	$0.6^{+0.4}_{-0.3}$	$0.0^{+0.2}_{-0.0}$	$0.00^{+0.24}_{-0.00}$
ee estimated	27^{+12}_{-12}	$0.7^{+0.4}_{-0.3}$	$0.6^{+0.4}_{-0.2}$	$0.02^{+0.01}_{-0.01}$
ee actual	22^{+7}_{-5}	$0.3^{+0.3}_{-0.1}$	$1.0^{+1.4}_{-0.7}$	$0.00^{+0.58}_{-0.00}$
$\mu\mu$ estimated	4^{+2}_{-2}	$0.08^{+0.06}_{-0.06}$	$0.05^{+0.04}_{-0.04}$	$0.004^{+0.003}_{-0.003}$
$\mu\mu$ actual	10^{+7}_{-4}	$0.11^{+0.21}_{-0.07}$	$0.06^{+0.21}_{-0.06}$	$0.078^{+0.210}_{-0.078}$

7.6 Additional studies

In addition, we perform several studies to check for other potential sources of background in the SRs. First, we invert the criterion that rejects material interactions and find no events in the SRs in data, across all channels and years. Thus, background from material interactions is not significant after the full selection criteria are applied. Second, we invert the cosmic-ray muon rejection criteria in the $\mu\mu$ channel and scale the number of events by the efficiency of cosmic-ray muon events to survive the cosmic-ray muon rejection criteria, which is found from a dedicated data sample of cosmic-ray muon events. With this study, we find a negligible number of cosmic-ray muon events.

To estimate an upper limit on the amount of heavy-flavor background in the signal region, several studies are performed. First, we perform the nominal ABCD method while additionally requiring at least one medium CSVv2 b-tagged jet [56]. In the $\mu\mu$ channel, which has the smallest relative SR contribution from mismeasurements and thus the most sensitivity to heavy-flavor backgrounds, we find that the estimate with at least one b-tagged jet is about an order of magnitude smaller than the nominal prediction, and thus negligible. In the second study of the heavy-flavor background in the signal region, we look at samples in which we invert the isolation criterion for events that pass the $\mu\mu$ preselection, for data and simulated background from SM events comprised uniquely of jets produced through the strong interaction, referred to as quantum chromodynamics (QCD) multijet events. These samples are dominated by muons from decays of B mesons, and the QCD multijet simulation describes the data well in the region outside of the Z boson peak in the invariant mass distribution. We perform a naive ABCD estimate with the QCD multijet simulation and find no evidence for $|d_0|$ correlation, which indicates that the nominal background estimation already accounts for the

heavy-flavor background. In the last heavy-flavor background study, we estimate this particular background in the SRs from the ratios of the number of events in each SR to the number of events in the prompt control region, from the QCD multijet simulation in the nonisolated region. We multiply these ratios by a normalization factor obtained from the number of QCD multijet simulated events that pass the nominal $\mu\mu$ preselection. Using this approach, we estimate that the heavy-flavor background is about 2% (20%) of the nominal background estimate in SR I (SR IV), which is small and well covered within the nominal prediction uncertainties.

A final potential background in the SRs is from leptonic decays of long-lived, low-mass SM hadrons. We examine 2018 data and QCD multijet simulation in the $\mu\mu$ channel with both the muon isolation and the ΔR requirements inverted to find a region dominated by low-mass events, which has clear contributions from the J/ψ, ψ', and Υ mesons. From data in this region, we find the ratios of the number of events in each SR to the number of events in the prompt control region. We multiply these ratios by a normalization factor found from QCD multijet simulated events and find that the low-mass SM contribution is less than 0.2% of the nominal prediction in SR I, which is negligible, and about 17% of the nominal prediction in SR IV, which is small and well covered by the large systematic uncertainty in this SR.

8 Systematic uncertainties in the signal efficiency

The systematic uncertainty in the background estimation method is the most important in the analysis: varying the nuisance parameter by one standard deviation shifts the best-fit signal strength by about 5%. The rest of the systematic uncertainties are applied to the signal efficiency.

The integrated luminosities of the 2016, 2017, and 2018 data-taking periods are individually known with uncertainties in the 1.2–2.5% range [57–59], which combined for the data set used in this analysis has a total uncertainty of 1.8%, the improvement in precision reflecting the uncorrelated time evolution of some systematic effects.

The simulation of pileup events assumes a total inelastic pp cross section of 69.2 mb, with an associated uncertainty of 5% [60]. The systematic uncertainty arising as a result of the modeling of pileup events is estimated by varying the cross section of the minimum-bias events by 5% when generating the target pileup distributions. The pileup weights are recomputed with these new distributions and applied to the simulated events to obtain the variation in the yields in the inclusive signal region. The average uncertainty is between 1 and 2%. We treat these uncertainties as 100% correlated across the three years of data taking.

The trigger efficiency systematic uncertainty is given by the uncertainty in the measured trigger efficiency scale factors. These uncertainties are about 1% for the $\mathrm{e}\mu$ and $\mu\mu$ channels and 10–19% for the ee channel. The uncertainty is larger for the ee channel relative to the other two channels because there are fewer events available for the efficiency measurement in this channel. In addition, to cover the change observed in the muon trigger efficiency in signal simulation over the full $|d_0|$ range, we assign an additional 20% uncertainty. We treat these uncertainties as 100% correlated across the three years of data taking.

The efficiency to reconstruct displaced, isolated, high p_{T} muons can be measured using cosmic-ray muon events, as they also have these properties. The tracking efficiency of displaced muons is measured using cosmic-ray events in simulation and data, and this efficiency is also used as a proxy for the tracking efficiency for displaced electrons. We take the difference in the mean efficiency between data and simulation as a systematic uncertainty in the signal yield. This

uncertainty is 2–14%, depending on the data-taking year. The 2017 and 2018 systematic uncertainties are treated as fully correlated, while the 2016 uncertainty is treated as uncorrelated with the 2017 and 2018 uncertainties, since the pixel detector was upgraded after the 2016 data taking.

One selection within the muon identification could have some dependence with respect to $|d_0|$, namely, the requirement that the muons have at least one pixel hit. We find the efficiency of this criterion in simulated cosmic-ray events and cosmic-ray events from data, and we apply the difference in mean efficiency between data and simulation as a systematic uncertainty in the signal yield. The average uncertainty is about 16% (32%) in the eμ ($\mu\mu$) channel. The 2017 and 2018 systematic uncertainties are treated as fully correlated, while the 2016 uncertainty is treated as uncorrelated with the 2017 and 2018 uncertainties.

For the two systematic uncertainties derived with cosmic-ray muon events, the largest uncertainty is in 2016, compared with relatively smaller uncertainties in 2017 and 2018. This is in part because the 2016 cosmic data sample is much smaller, meaning that the statistical uncertainties are larger in this year. In addition, the uncertainty is reduced in 2017 and 2018 due to the upgrade of the pixel tracker, which allows for more precise tracking measurements.

To find the systematic uncertainty associated with the corrections to the lepton identification and isolation, we fluctuate the lepton scale factors up and down by their uncertainty and observe the change in the event yields in the inclusive signal region. The average uncertainty for electrons is about 3% in the eμ channel and about 7% in the ee channel, while the average uncertainty for muons is $<$1%. We treat these uncertainties as 100% correlated across the three years of data taking.

To find the systematic uncertainty associated with the corrections to the lepton $|d_0|$, we fluctuate the lepton $|d_0|$ corrections up and down by their uncertainty and observe the change in the event yields in the inclusive signal region. We find that this uncertainty is negligible in 2017 and 2018, and there is no $|d_0|$ correction needed for the 2016 simulation.

The systematic uncertainties in the signal efficiency are summarized in Table 5.

Table 5: Systematic uncertainties in the signal efficiency, for all three years and the three channels. For many sources of uncertainty, a range indicating the 68% CL of the spread is given, followed by the mean. Uncertainties in the same row are treated as correlated among the years of data taking, except for the displaced tracking and muon pixel hit efficiencies, where the 2016 uncertainty is treated as uncorrelated with the 2017 and 2018 uncertainties.

Systematic uncertainty	2016	2017	2018
Integrated luminosity		1.8% (2016–2018)	
Pileup			
- eμ channel	0.2–0.7% / 0.5%	0.4–0.9% / 0.6%	0.3–0.7% / 0.5%
- ee channel	0.1–0.9% / 0.5%	0.5–1.2% / 0.9%	0.4–1.2% / 0.8%
- $\mu\mu$ channel	0–0.4% / 0.2%	0–0.3% / 0.1%	0–0.4% / 0.2%
Trigger efficiency			
- eμ channel, electrons	1.6%	1.3%	1.2%
- eμ channel, muons	1.6%	1.4%	1.2%
- ee channel	10%	13%	19%
- $\mu\mu$ channel	1.2%	1.0%	1.1%
Muon trigger efficiency at large $\lvert d_0 \rvert$			
- eμ channel, muons	20%	20%	20%
- $\mu\mu$ channel	20%	20%	20%
Displaced tracking efficiency	14%	5.8%	2.4%
Muon pixel hit efficiency			
- eμ channel, muons	30–32% / 32%	10–13% / 12%	12–17% / 16%
- $\mu\mu$ channel	70–74% / 73%	20–24% / 23%	27–31% / 30%
Lepton identification and isolation			
- eμ channel, electrons	1.2–1.3% / 1.2%	3.1–4.0% / 3.6%	3.1–3.9% / 3.5%
- eμ channel, muons	0.04–0.05% / 0.05%	0.06–0.07% / 0.07%	0.05–0.06% / 0.06%
- ee channel	2.3–2.5% / 2.4%	6.4–7.9% / 7.2%	6.3–7.7% / 7.0%
- $\mu\mu$ channel	0.09–0.10% / 0.10%	0.14–0.15% / 0.14%	0.11–0.13% / 0.12%

9 Results

Figure 3 shows the expected number of background events and the observed data, with a representative signal overlaid, in each p_T bin and each SR, for each channel. We split SR I into two bins. In the eμ and $\mu\mu$ channels, these bins are in the leading muon p_T, and in the ee channel, these bins are in the leading electron p_T. The bin boundary is at 90 (140) GeV for the 2016 (2017+2018) eμ channel, at 300 (400) GeV for the 2016 (2017+2018) ee channel, and at 100 GeV for all years in the $\mu\mu$ channel. The p_T bins are chosen such that the bin with higher p_T contains less than one background event, which maximizes the sensitivity to small lifetimes. The observed number of events is consistent with the predicted amount of background. The observed significance is found to be $\leq$2 for all signal points, for each analysis channel as well as the channel combination.

In the high p_T SR I bin, which is the most sensitive bin for large top squark masses and small $c\tau_0$ values, particularly $c\tau_0 \lessapprox 1$ cm, the eμ channel has the largest signal yield relative to the other two channels. As described above, this is because there are twice as many chances to have one electron and one muon, since the top squarks decay to each lepton flavor with equal probability. In this bin, the ee and $\mu\mu$ channel signal yields are similar. In SR IV, which is the most sensitive bin for large top squark masses and large lifetimes, the $\mu\mu$ channel has the largest signal yield for $c\tau_0 \gtrapprox 10$ cm, relative to the other two channels. This is because the muon reconstruction and selection efficiency is better than that of electrons, which is particularly true at large $\lvert d_0 \rvert$.

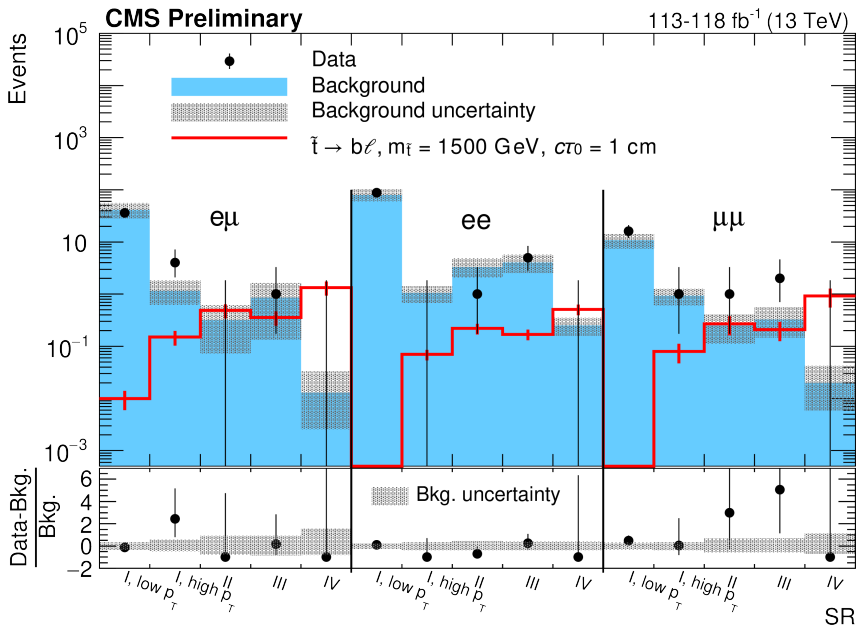

Figure 3: The number of estimated background and observed events in each channel and SR, with a representative signal overlaid. For each background estimate and signal yield, the total uncertainty (statistical plus systematic) is given. The distributions shown are those obtained before the final maximum likelihood fit to the data.

In this bin, the eμ and $\mu\mu$ channels have similar amounts of background, and the ee channel has the smallest signal yield out of the three channels, for $c\tau_0 \gtrapprox 10$ cm. Therefore, for large top squark masses, the eμ channel is the most sensitive for $c\tau_0 \lessapprox 10$ cm, the $\mu\mu$ channel is the most sensitive for $c\tau_0 \gtrapprox 10$ cm, and the ee channel is the least sensitive of the three for $c\tau_0 \gtrapprox 10$ cm.

We perform a simultaneous counting experiment in each signal region bin for most of the interpretations we consider. However, the ee and $\mu\mu$ channels are fit individually to calculate limits on GMSB models with a $\tilde{e}$ or $\tilde{\mu}$ NLSP. We set upper limits on the product of the signal production cross section and branching fraction to leptons ($\mathcal{B}\sigma$) [61–64]. By comparing the expected and observed cross section limits to the theoretical cross sections at next-to-leading order, mass and $c\tau_0$ exclusion limits are set for each of the models we consider. Figures 4, 5, and 6 show the 95% confidence level (CL) upper limits for the top squarks, sleptons, and exotic Higgs bosons, respectively. The top squark limits assume $\mathcal{B}(\tilde{t} \to b\ell) = \mathcal{B}(\tilde{t} \to d\ell) = 100\%$, and each lepton has an equal probability of being an electron, a muon, or a tau lepton. The slepton limits assume that the superpartners of the left- and right-handed leptons are degenerate in mass. The Higgs boson limits assume that the mass of S is 30 or 50 GeV, $\mathcal{B}(H \to SS) = 100\%$, and each S has an equal probability of decaying to two electrons or two muons. In Figs. 4 and 5, the area to the left of the solid curves represents the observed exclusion region, and the dashed lines indicate the expected limits. We exclude $\tilde{t}$ masses up to 1500 GeV at a $c\tau_0$ of 2 cm, which indicates the maximum sensitivity of this search. The sensitivity degrades for $\tilde{t}$ masses and $c\tau_0$ values above and below this point. The previous CMS analysis, which was performed only in the eμ channel and at a center-of-mass energy of 8 TeV, excluded $\tilde{t}$ masses up to 790 GeV at a $c\tau_0$ of 2 cm. Thus, this analysis shows a clear improvement in the results with respect to the previous analysis. Furthermore, this search can be directly compared with the search described in Ref. [14], which looks for displaced leptons with the ATLAS detector at a center-of-mass energy of 13 TeV. The smaller $|d_0|$ lower bound of the SRs enables this analysis to have greater sensitivity to small slepton lifetimes than the ATLAS analysis.

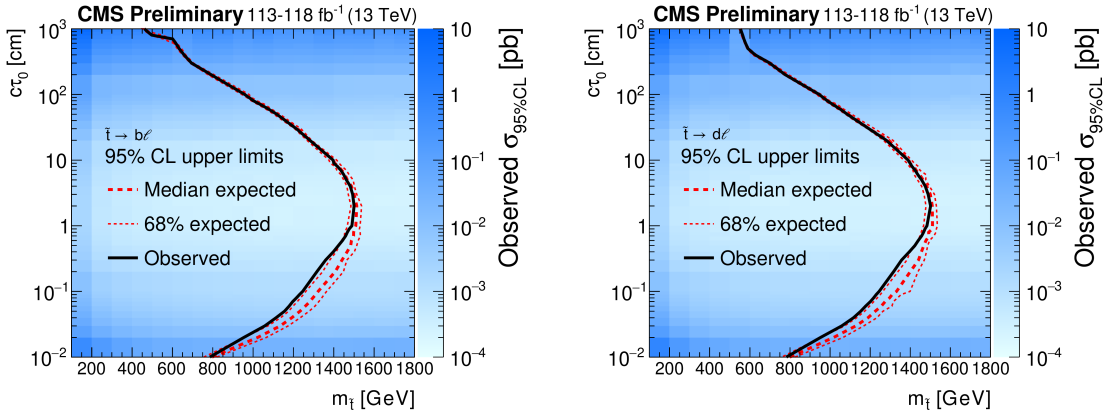

Figure 4: The observed 95% CL upper limits on the long-lived top squark production cross section, in the $c\tau_0$ – mass plane, for the three channels combined. The $\widetilde{\mathrm{t}}\widetilde{\mathrm{t}} \to \overline{\ell}\mathrm{b}\,\ell\overline{\mathrm{b}}$ (left) and $\widetilde{\mathrm{t}}\widetilde{\mathrm{t}} \to \overline{\ell}\mathrm{d}\,\ell\overline{\mathrm{d}}$ (right) processes are shown. The area to the left of the black curve represents the observed exclusion region, and the dashed red lines indicate the expected limits and their 68% CLs.

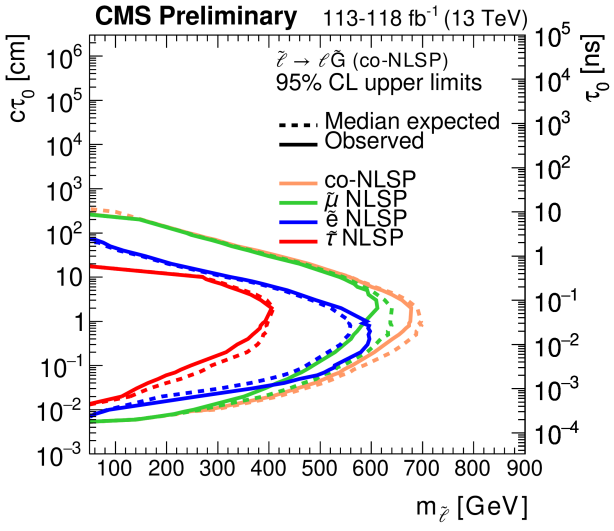

Figure 5: The 95% CL upper limits on the long-lived slepton production cross section, in the $c\tau_0$ – mass plane. The $\widetilde{\tau}$ and co-NLSP limits are shown for the three channels combined, while the $\widetilde{\mathrm{e}}$ and $\widetilde{\mu}$ NLSP limits are shown for the ee and $\mu\mu$ channels, respectively. The area to the left of the solid curves represents the observed exclusion region, and the dashed lines indicate the expected limits.

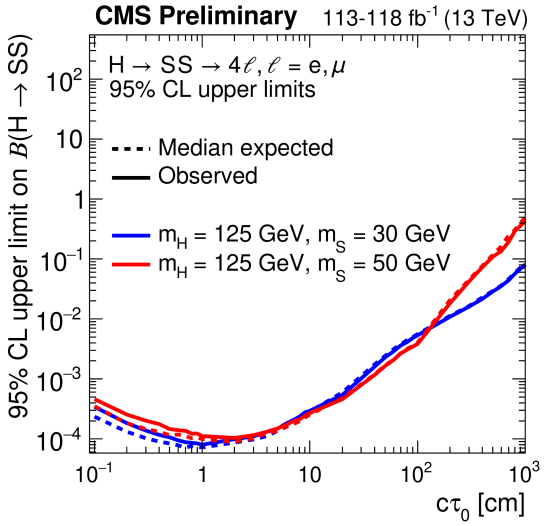

Figure 6: The 95% CL upper limits on the H $\rightarrow$ SS $\rightarrow \ell\bar{\ell}\,\ell\bar{\ell}$ branching fraction as a function of $c\tau_0$, for a Higgs boson with a mass of 125 GeV and a long-lived scalar with a mass of 30 GeV or 50 GeV, for the three channels combined. The area above the solid (dashed) curve represents the observed (expected) exclusion region.

10 Summary

A search has been presented for long-lived particles decaying to displaced leptons in proton-proton collisions at a center-of-mass energy of 13 TeV at the CERN LHC. With collision data recorded in 2016, 2017, and 2018, and corresponding to an integrated luminosity of 113–118 fb^{-1}, no excess above the estimated background has been observed. Upper limits have been set at 95% confidence level. Top squarks with masses between 100 and at least 460 GeV have been excluded for proper decay lengths between 0.01 and 1000 cm, with a maximum exclusion of 1500 GeV occurring at a proper decay length of 2 cm, assuming 100% of the top squarks decay to a lepton and a b or d quark, where the lepton has an equal probability of being an electron, muon, or tau lepton. The following exclusions assume that the superpartners of the left- and right-handed leptons are mass degenerate. Electron superpartners with masses of at least 50 GeV have been excluded for proper decay lengths between 0.007 and 70 cm, with a maximum exclusion of 610 GeV occurring at a proper decay length of 0.7 cm. Muon superpartners with masses of at least 50 GeV have been excluded for proper decay lengths between 0.005 and 265 cm, with a maximum exclusion of 610 GeV occurring at a proper decay length of 3 cm. Tau lepton superpartners with masses of at least 50 GeV have been excluded for proper decay lengths between 0.015 and 20 cm, with a maximum exclusion of 405 GeV occurring at a proper decay length of 2 cm. In the case that electron, muon, and tau lepton superpartners are mass degenerate, lepton superpartners with masses between 50 and at least 270 GeV have been excluded for proper decay length between 0.005 and 265 cm, with a maximum exclusion of 680 GeV occurring at a proper decay length of 2 cm. For proper decay lengths between 0.10 and 12 cm, Higgs bosons with a mass of 125 GeV and with branching ratios to two long-lived scalars greater than 0.03% have been excluded, assuming each scalar has a mass of 30 GeV and decays with equal probability to electrons or muons. This is the first search at CMS for dis-

placed leptons at a center-of-mass energy of 13 TeV, and the first search at CMS for displaced leptons in the electron-electron and muon-muon channels that does not require the leptons to come from a common displaced vertex. As a result of the larger center-of-mass energy and integrated luminosity, as well as the addition of the same-flavor channels, the mass exclusion limits for this search improve upon previous CMS results by approximately a factor of 2.

References

[1] ATLAS Collaboration, "Search for magnetic monopoles and stable high-electric-charge objects in 13 TeV proton-proton collisions with the ATLAS detector", *Phys. Rev. Lett.* **124** (2020) 031802, doi:10.1103/PhysRevLett.124.031802, arXiv:1905.10130.

[2] ATLAS Collaboration, "Search for heavy charged long-lived particles in the ATLAS detector in 36.1 fb^{-1} of proton-proton collision data at $\sqrt{s} = 13$ TeV", *Phys. Rev. D* **99** (2019) 092007, doi:10.1103/PhysRevD.99.092007, arXiv:1902.01636.

[3] CMS Collaboration, "Search for disappearing tracks in proton-proton collisions at $\sqrt{s} =$ 13 TeV", *Phys. Lett. B* **806** (2020) 135502, doi:10.1016/j.physletb.2020.135502, arXiv:2004.05153.

[4] CMS Collaboration, "Searches for physics beyond the standard model with the M_{T2} variable in hadronic final states with and without disappearing tracks in proton-proton collisions at $\sqrt{s} = 13$ TeV", *Eur. Phys. J. C* **80** (2020) 3, doi:10.1140/epjc/s10052-019-7493-x, arXiv:1909.03460.

[5] ATLAS Collaboration, "Search for long-lived charginos based on a disappearing-track signature in pp collisions at $\sqrt{s} = 13$ TeV with the ATLAS detector", *JHEP* **06** (2018) 022, doi:10.1007/JHEP06(2018)022, arXiv:1712.02118.

[6] CMS Collaboration, "Search for long-lived particles using displaced jets in proton-proton collisions at $\sqrt{s} = 13$ TeV", 2020. arXiv:2012.01581. Submitted to *Phys. Rev. D*.

[7] CMS Collaboration, "Search for long-lived particles using nonprompt jets and missing transverse momentum with proton-proton collisions at $\sqrt{s} = 13$ TeV", *Phys. Lett. B* **797** (2019) 134876, doi:10.1016/j.physletb.2019.134876, arXiv:1906.06441.

[8] ATLAS Collaboration, "Search for long-lived neutral particles in pp collisions at $\sqrt{s} = 13$ TeV that decay into displaced hadronic jets in the ATLAS calorimeter", *Eur. Phys. J. C* **79** (2019) 481, doi:10.1140/epjc/s10052-019-6962-6, arXiv:1902.03094.

[9] ATLAS Collaboration, "Search for long-lived particles produced in pp collisions at $\sqrt{s} = 13$ TeV that decay into displaced hadronic jets in the ATLAS muon spectrometer", *Phys. Rev. D* **99** (2019) 052005, doi:10.1103/PhysRevD.99.052005, arXiv:1811.07370.

[10] ATLAS Collaboration, "Search for long-lived neutral particles produced in pp collisions at $\sqrt{s} = 13$ TeV decaying into displaced hadronic jets in the ATLAS inner detector and muon spectrometer", *Phys. Rev. D* **101** (2020) 052013, doi:10.1103/PhysRevD.101.052013, arXiv:1911.12575.

[11] CMS Collaboration, "Search for long-lived particles using delayed photons in proton-proton collisions at $\sqrt{s} = 13$ TeV", *Phys. Rev. D* **100** (2019) 112003, doi:10.1103/PhysRevD.100.112003, arXiv:1909.06166.

[12] ATLAS Collaboration, "Search for nonpointing and delayed photons in the diphoton and missing transverse momentum final state in 8 TeV pp collisions at the LHC using the ATLAS detector", *Phys. Rev. D* **90** (2014) 112005, doi:10.1103/PhysRevD.90.112005, arXiv:1409.5542.

[13] CMS Collaboration, "Search for long-lived particles that decay into final states containing two electrons or two muons in proton-proton collisions at $\sqrt{s} = 8$ TeV", *Phys. Rev. D* **91** (2015) 052012, doi:10.1103/PhysRevD.91.052012, arXiv:1411.6977.

[14] ATLAS Collaboration, "Search for displaced leptons in $\sqrt{s} = 13$ TeV pp collisions with the ATLAS detector", 2020. arXiv:2011.07812. Submitted to *Phys. Rev. Lett.*

[15] ATLAS Collaboration, "Search for heavy neutral leptons in decays of W bosons produced in 13 TeV pp collisions using prompt and displaced signatures with the ATLAS detector", *JHEP* **10** (2019) 265, doi:10.1007/JHEP10(2019)265, arXiv:1905.09787.

[16] ATLAS Collaboration, "Search for long-lived, massive particles in events with a displaced vertex and a muon with large impact parameter in pp collisions at $\sqrt{s} = 13$ TeV with the ATLAS detector", *Phys. Rev. D* **102** (2020) 032006, doi:10.1103/PhysRevD.102.032006, arXiv:2003.11956.

[17] ATLAS Collaboration, "Search for displaced vertices of oppositely charged leptons from decays of long-lived particles in pp collisions at $\sqrt{s}$ =13 TeV with the ATLAS detector", *Phys. Lett. B* **801** (2020) 135114, doi:10.1016/j.physletb.2019.135114, arXiv:1907.10037.

[18] CMS Collaboration, "Search for decays of stopped exotic long-lived particles produced in proton-proton collisions at $\sqrt{s} = 13$ TeV", *JHEP* **05** (2018) 127, doi:10.1007/JHEP05(2018)127, arXiv:1801.00359.

[19] ATLAS Collaboration, "Search for light long-lived neutral particles produced in pp collisions at $\sqrt{s} = 13$ TeV and decaying into collimated leptons or light hadrons with the ATLAS detector", *Eur. Phys. J. C* **80** (2020) 450, doi:10.1140/epjc/s10052-020-7997-4, arXiv:1909.01246.

[20] CMS Collaboration, "Search for displaced supersymmetry in events with an electron and a muon with large impact parameters", *Phys. Rev. Lett.* **114** (2015) 061801, doi:10.1103/PhysRevLett.114.061801, arXiv:1409.4789.

[21] P. Graham, D. Kaplan, S. Rajendran, and P. Sarawat, "Displaced supersymmetry", *JHEP* **07** (2012) 149, doi:10.1007/JHEP07(2012)149, arXiv:1204.6038.

[22] R. Barbier et al., "R-parity violating supersymmetry", *Phys. Rept.* **420** (2005) 1, doi:10.1016/j.physrep.2005.08.006, arXiv:hep-ph/0406039.

[23] J. A. Evans and J. Shelton, "Long-lived staus and displaced leptons at the LHC", *JHEP* **04** (2016) 056, doi:10.1007/JHEP04(2016)056, arXiv:1601.01326.

[24] M. J. Strassler and K. M. Zurek, "Discovering the Higgs through highly-displaced vertices", *Phys. Lett. B* **661** (2008) 263, doi:10.1016/j.physletb.2008.02.008, arXiv:hep-ph/0605193.

[25] CMS Tracker Group Collaboration, "The CMS Phase-1 pixel detector upgrade", *JINST* **16** (2021) P02027, doi:10.1088/1748-0221/16/02/P02027, arXiv:2012.14304.

[26] CMS Collaboration, "Track impact parameter resolution for the full pseudo rapidity coverage in the 2017 dataset with the CMS Phase-1 pixel detector", CMS Detector Performance Summary CMS-DP-2020-049, 2020.

[27] CMS Collaboration, "Description and performance of track and primary-vertex reconstruction with the CMS tracker", *JINST* **9** (2014) P10009, doi:10.1088/1748-0221/9/10/P10009, arXiv:1405.6569.

[28] CMS Collaboration, "Performance of the CMS Level-1 trigger in proton-proton collisions at $\sqrt{s} = 13\,\text{TeV}$", *JINST* **15** (2020) P10017, doi:10.1088/1748-0221/15/10/P10017, arXiv:2006.10165.

[29] CMS Collaboration, "The CMS trigger system", *JINST* **12** (2017) P01020, doi:10.1088/1748-0221/12/01/P01020, arXiv:1609.02366.

[30] CMS Collaboration, "Performance of the CMS muon trigger system in proton-proton collisions at $\sqrt{s} = 13$ TeV", *JINST* **16** (2021) P07001, doi:10.1088/1748-0221/16/07/P07001, arXiv:2102.04790.

[31] CMS Collaboration, "The CMS experiment at the CERN LHC", *JINST* **3** (2008) S08004, doi:10.1088/1748-0221/3/08/S08004.

[32] NNPDF Collaboration, "Parton distributions for the LHC Run II", *JHEP* **04** (2015) 040, doi:10.1007/JHEP04(2015)040, arXiv:1410.8849.

[33] CMS Collaboration, "Event generator tunes obtained from underlying event and multiparton scattering measurements", *Eur. Phys. J. C* **76** (2016) 155, doi:10.1140/epjc/s10052-016-3988-x, arXiv:1512.00815.

[34] CMS Collaboration, "Extraction and validation of a new set of CMS PYTHIA8 tunes from underlying-event measurements", *Eur. Phys. J. C* **80** (2020) 4, doi:10.1140/epjc/s10052-019-7499-4, arXiv:1903.12179.

[35] GEANT4 Collaboration, "GEANT4—a simulation toolkit", *Nucl. Instrum. Meth. A* **506** (2003) 250, doi:10.1016/S0168-9002(03)01368-8.

[36] J. Alwall et al., "The automated computation of tree-level and next-to-leading order differential cross sections, and their matching to parton shower simulations", *JHEP* **07** (2014) 079, doi:10.1007/JHEP07(2014)079, arXiv:1405.0301.

[37] R. Frederix and S. Frixione, "Merging meets matching in MC@NLO", *JHEP* **12** (2012) 061, doi:10.1007/JHEP12(2012)061, arXiv:1209.6215.

[38] J. Alwall et al., "Comparative study of various algorithms for the merging of parton showers and matrix elements in hadronic collisions", *Eur. Phys. J. C* **53** (2008) 473, doi:10.1140/epjc/s10052-007-0490-5, arXiv:0706.2569.

[39] S. Frixione and B. R. Webber, "Matching NLO QCD computations and parton shower simulations", *JHEP* **06** (2002) 029, doi:10.1088/1126-6708/2002/06/029, arXiv:hep-ph/0204244.

[40] P. Nason, "A new method for combining NLO QCD with shower Monte Carlo algorithms", *JHEP* **11** (2004) 040, doi:10.1088/1126-6708/2004/11/040, arXiv:hep-ph/0409146.

[41] S. Frixione, P. Nason, and C. Oleari, "Matching NLO QCD computations with parton shower simulations: the POWHEG method", *JHEP* **11** (2007) 070, doi:10.1088/1126-6708/2007/11/070, arXiv:0709.2092.

[42] S. Alioli, P. Nason, C. Oleari, and E. Re, "NLO vector-boson production matched with shower in POWHEG", *JHEP* **07** (2008) 060, doi:10.1088/1126-6708/2008/07/060, arXiv:0805.4802.

[43] S. Alioli, P. Nason, C. Oleari, and E. Re, "A general framework for implementing NLO calculations in shower Monte Carlo programs: the POWHEG BOX", *JHEP* **06** (2010) 043, doi:10.1007/JHEP06(2010)043, arXiv:1002.2581.

[44] T. Sjöstrand et al., "An introduction to PYTHIA 8.2", *Comput. Phys. Commun.* **191** (2015) 159, doi:10.1016/j.cpc.2015.01.024, arXiv:1410.3012.

[45] R. Mackeprang and A. Rizzi, "Interactions of coloured heavy stable particles in matter", *Eur. Phys. J. C* **50** (2007) 353, doi:10.1140/epjc/s10052-007-0252-4, arXiv:hep-ph/0612161.

[46] R. Mackeprang and D. Milstead, "An updated description of heavy-hadron interactions in GEANT-4", *Eur. Phys. J. C* **66** (2010) 493, doi:10.1140/epjc/s10052-010-1262-1, arXiv:0908.1868.

[47] CMS Collaboration, "Performance of electron reconstruction and selection with the CMS detector in proton-proton collisions at $\sqrt{s} = 8\,\text{TeV}$", *JINST* **10** (2015) P06005, doi:10.1088/1748-0221/10/06/P06005, arXiv:1502.02701.

[48] CMS Collaboration, "Electron and photon reconstruction and identification with the CMS experiment at the CERN LHC", *JINST* **16** (2021) P05014, doi:10.1088/1748-0221/16/05/P05014, arXiv:2012.06888.

[49] CMS Collaboration, "Performance of the CMS muon detector and muon reconstruction with proton-proton collisions at $\sqrt{s} = 13\,\text{TeV}$", *JINST* **13** (2018) P06015, doi:10.1088/1748-0221/13/06/P06015, arXiv:1804.04528.

[50] CMS Collaboration, "Particle-flow reconstruction and global event description with the CMS detector", *JINST* **12** (2017) P10003, doi:10.1088/1748-0221/12/10/P10003, arXiv:1706.04965.

[51] M. Cacciari, G. P. Salam, and G. Soyez, "The anti-k_{T} jet clustering algorithm", *JHEP* **04** (2008) 063, doi:10.1088/1126-6708/2008/04/063, arXiv:0802.1189.

[52] M. Cacciari, G. P. Salam, and G. Soyez, "FastJet user manual", *Eur. Phys. J. C* **72** (2012) 1896, doi:10.1140/epjc/s10052-012-1896-2, arXiv:1111.6097.

[53] CMS Collaboration, "Precision measurement of the structure of the CMS inner tracking system using nuclear interactions", *JINST* **13** (2018) P10034, doi:10.1088/1748-0221/13/10/P10034, arXiv:1807.03289.

[54] R. Fruhwirth, "Application of Kalman filtering to track and vertex fitting", *Nucl. Instrum. Meth. A* **262** (1987) 444, doi:10.1016/0168-9002(87)90887-4.

[55] R. Fruhwirth, P. Kubinec, W. Mitaroff, and M. Regler, "Vertex reconstruction and track bundling at the LEP collider using robust algorithms", *Comput. Phys. Commun.* **96** (1996) 189, doi:10.1016/0010-4655(96)00040-9.

[56] CMS Collaboration, "Identification of heavy-flavour jets with the CMS detector in pp collisions at 13 TeV", *JINST* **13** (2018) P05011, doi:10.1088/1748-0221/13/05/P05011, arXiv:1712.07158.

[57] CMS Collaboration, "Precision luminosity measurement in proton-proton collisions at $\sqrt{s} = 13$ TeV in 2015 and 2016 at CMS", 2021. arXiv:2104.01927. Submitted to *Eur. Phys. J. C*.

[58] CMS Collaboration, "CMS luminosity measurements for the 2017 data-taking period at $\sqrt{s} = 13$ TeV", CMS Physics Analysis Summary CMS-PAS-LUM-17-004, 2018.

[59] CMS Collaboration, "CMS luminosity measurements for the 2018 data-taking period at $\sqrt{s} = 13$ TeV", CMS Physics Analysis Summary CMS-PAS-LUM-18-002, 2018.

[60] CMS Collaboration, "Measurement of the inelastic proton-proton cross section at $\sqrt{s} = 13$ TeV", *JHEP* **07** (2018) 161, doi:10.1007/JHEP07(2018)161, arXiv:1802.02613.

[61] T. Junk, "Confidence level computation for combining searches with small statistics", *Nucl. Instrum. Meth. A* **434** (1999) 435, doi:10.1016/S0168-9002(99)00498-2, arXiv:hep-ex/9902006.

[62] A. L. Read, "Presentation of search results: The CL_s technique", *J. Phys. G* **28** (2002) 2693, doi:10.1088/0954-3899/28/10/313.

[63] G. Cowan, K. Cranmer, E. Gross, and O. Vitells, "Asymptotic formulae for likelihood-based tests of new physics", *Eur. Phys. J. C* **71** (2011) 1554, doi:10.1140/epjc/s10052-011-1554-0, arXiv:1007.1727. [Erratum: doi:10.1140/epjc/s10052-013-2501-z].

[64] The ATLAS Collaboration, The CMS Collaboration, The LHC Higgs Combination Group, "Procedure for the LHC Higgs boson search combination in Summer 2011", Technical Report CMS-NOTE-2011-005, ATL-PHYS-PUB-2011-11, 2011.